Ultrasonics 54 (2014) 1842–1850

Contents lists available at ScienceDirect

Ultrasonics

journal homepage: www.elsevier.com/locate/ultras

A comparison between ultrasonic array beamforming and super resolution imaging algorithms for non-destructive evaluation ☆

Chengguang Fan [a,b], Mihai Caleap [b], Mengchun Pan [a], Bruce W. Drinkwater [b,*]

[a] College of Mechatronic Engineering and Automation, National University of Defense Technology, Changsha 410073, PR China
[b] Department of Mechanical Engineering, University of Bristol, Queen's Building, University Walk, Bristol BS8 1TR, UK

ARTICLE INFO

Article history:
Received 29 August 2013
Received in revised form 5 December 2013
Accepted 23 December 2013
Available online 8 January 2014

Keywords:
Ultrasonic array
Modelling
Post processing
Lateral resolution
Noise

ABSTRACT

In this paper the total focusing method, the so called gold standard in classical beamforming, is compared with the widely used time-reversal MUSIC super resolution technique in terms of its ability to resolve closely spaced scatterers in a solid. The algorithms are tested with simulated and experimental array data, each containing different noise levels. The performance of the algorithms is evaluated in terms of lateral resolution and sensitivity to noise. It is shown that for the weak noise situation (SNR > 20 dB), time-reversal MUSIC provides significantly enhanced lateral resolution when compared to the total focusing method, breaking the diffraction limit. However, for higher noise levels, the total focusing method is shown to be robust, whilst the performance of time-reversal MUSIC is degraded. The influence of multiple scattering on the imaging algorithms is also investigated and shown to be small.

1. Introduction

The use of ultrasonic arrays for industrial non-destructive evaluation (NDE) has dramatically increased in recent years [1,2]. Compared to traditional single element transducers, ultrasonic arrays offer two main advantages. Firstly, an ultrasonic array is more versatile than a single element transducer, which means the ultrasonic array is able to undertake a range of different inspections from a single location. Secondly, an ultrasonic array can be used to produce images at each test location and hence the potential exists for accurate detection and characterisation. For these reasons arrays have found widespread use, especially in the aerospace and nuclear industrial sectors. Much of the industrial imaging for NDE uses linear (one-dimensional) arrays to produce two-dimensional cross-sectional images. The more recent development of two-dimensional arrays to facilitate three-dimensional imaging [3–5] allows the internal structures of engineering components to be even more realistically visualised. Flexible arrays [6,7] and air-coupled arrays [8,9] allow the rapid testing of components with complex geometries.

In traditional array imaging, beamforming is used in which the array elements are excited in a predefined sequence, termed the delay law, to form a coherent beam. The received signals are then processed to form an image, often using the same array elements, obeying the same delay law [10]. Alternatively and equivalently, the complete time-domain data from each possible transmitter-receiver element pair, termed Full Matrix Capture (FMC), can be recorded and an imaging algorithm applied to this data as a post-processing operation [11,12]. Notable delay and sum based post-processing imaging algorithms are the synthetic aperture focusing technique (SAFT) [13,14], inverse wave-field extrapolation [15,16] and the total focusing method (TFM) [17]. All these algorithms aim to produce high resolution images, but their resolution is diffraction limited. The diffraction limit has been challenged by progress made in optical microscopy and radar where near field [18] and far field [19,20] super resolution has been demonstrated. More recently super resolution has been demonstrated in ultrasonic imaging, in fluids (or tissue-mimicking phantoms) for medical imaging [21] as well as in solids of direct relevance to NDE [22].

Time-reversal methods have been widely applied to yield highly focused beams in applications such as the destruction of kidney stones [23], medical hyperthermia and brain therapy [24] as well as super resolution imaging [25–32]. There are many super resolution algorithms and in this paper we select the time-reversal MUSIC (multiple signal classification) algorithm [26–32], as this is arguably the most widely used in ultrasonic imaging. Davy et al. [32] considered the effect of noise for electromagnetic wave imaging and showed that at high noise levels super resolution is not achieved. Recently, a phase-coherent version of time-reversal MUSIC was proposed to further improve the resolution [33]. A general-

* Corresponding author. Tel.: +44 (0)117 3315914.
E-mail address: b.drinkwater@bristol.ac.uk (B.W. Drinkwater).

http://dx.doi.org/10.1016/j.ultras.2013.12.012
0041-624X/

ized time-reversal MUSIC algorithm accounting for attenuation in the medium and the finite-size effects of the transducer elements has been shown to yield even higher-resolution images [21]. Simonetti [34] highlighted the importance of multiple scattering in super resolution imaging, however its role is still an open question [35].

From the practical point of view it is unclear when and where TFM and/or time-reversal MUSIC should be used in NDE. For this reason the main aim of this paper is to compare the performance of TFM and time-reversal MUSIC in terms of their suitability for use in NDE. Both algorithms rely on the same array data as inputs and here we compare their performance in terms of lateral resolution and robustness to noise, two particularly important performance indicators for NDE imaging algorithms.

Section 2 of this paper describes a general model of ultrasonic array data, in which multiple scattering between different targets is considered. Section 3 gives an overview of the TFM and time-reversal MUSIC imaging algorithms. The performance indicators used to assess the imaging algorithms are then introduced. In Section 4, an experimental system is described to extract real NDE data, and the performance of these two imaging algorithms is discussed in terms of lateral resolution and robustness to noise.

2. Simulation of ultrasonic array data

This section describes the forward model used to simulate ultrasonic array data. The geometry is a planar linear array of N elements, located at $\boldsymbol{R}_l$ ($l = 1, 2, \ldots, N$), assumed to be in direct contact with a solid sample as shown schematically in Fig. 1. The elements are assumed to be long in the Y-direction and so the model is reduced to two-dimensions, with propagation of energy in the x–z plane only. Each array element radiates ultrasound into free space $z > 0$, in which are embedded two isotropic scatterers of size a centred at $\boldsymbol{r}_j$ ($j = 1, 2$). Note that the scatterers are also two-dimensional and hence represent, for example, side drilled holes. The distance between the scatterers is d. In the following, only longitudinal waves are considered. In this case the scalar potential ϕ can be used instead of the displacement vector $\boldsymbol{u}$, so that $\boldsymbol{u} = \nabla\phi$.

2.1. Forward model of the complete scattering process

If there is more than one scatterer, multiple scattering effects take place. In the neighbourhood of the each scatterer, the scattered field will behave as $E_jG(\boldsymbol{r}, \boldsymbol{r}_j)$, $j = 1, 2$, where E_j is an unknown complex amplitude and $G(\boldsymbol{r}, \boldsymbol{r}_j)$ is the free space Green's function at a point $\boldsymbol{r}$ in the field of a source at $\boldsymbol{r}_j$. We assume that the array elements emit monochromatic longitudinal waves of angular frequency, ω, propagating with wavenumber, $k = \omega/c_L$ and propagation is modelled using the simple Green's function below:

$$G(\boldsymbol{r}, \boldsymbol{r}_j) = -\frac{i}{4}H_0^{(1)}(k|\boldsymbol{r} - \boldsymbol{r}_j|), \tag{1}$$

where i is the imaginary unit and $H_0^{(1)}$ is a cylindrical Hankel function.

The multiple scattering process for two isotropic point scatterers is presented in the following form [36]:

$$\phi(\boldsymbol{r}) = \phi^{in}(\boldsymbol{r}) + E_1G(\boldsymbol{r}, \boldsymbol{r}_1) + E_2G(\boldsymbol{r}, \boldsymbol{r}_2). \tag{2}$$

The scattering properties of the scatterers are characterised by

$$E_j = f_j\phi_j^{ex}(\boldsymbol{r}_j), \quad (j = 1, 2), \tag{3}$$

where f_j denotes a scattering coefficient. The scattered field is determined by the value of the exciting field at $\boldsymbol{r}_j$ together with the amplification factor f_j. We assume that the scattering coefficients f_j are known. The exciting field ϕ_j^{ex} is regarded as the field incident on one scatterer, in presence of the other scatterer. Evaluation of the exciting field at $\boldsymbol{r}_1$ and $\boldsymbol{r}_2$ yields the following coupled linear system of equations:

$$\begin{cases} \phi_1^{ex}(\boldsymbol{r}_1) = \phi^{in}(\boldsymbol{r}_1) + f_2\phi_2^{ex}(\boldsymbol{r}_2)G(\boldsymbol{r}_1, \boldsymbol{r}_2), \\ \phi_2^{ex}(\boldsymbol{r}_2) = \phi^{in}(\boldsymbol{r}_2) + f_1\phi_1^{ex}(\boldsymbol{r}_1)G(\boldsymbol{r}_2, \boldsymbol{r}_1), \end{cases} \tag{4}$$

and the total field can be finally written as:

$$\phi(\boldsymbol{r}) = \phi^{in}(\boldsymbol{r}) + f_1\phi_1^{ex}(\boldsymbol{r}_1)G(\boldsymbol{r}, \boldsymbol{r}_1) + f_2\phi_2^{ex}(\boldsymbol{r}_2)G(\boldsymbol{r}, \boldsymbol{r}_2). \tag{5}$$

This solution contains all multiple scattering interactions between two isotropic point scatterers and is valid for any incident wave $\phi^{in}(\boldsymbol{r})$.

2.2. Simulated ultrasonic array data

Simulations were performed to model the ultrasonic array data when each array element shown in Fig. 1 is excited sequentially and the backscattered signals are recorded by all elements. The forward model was used to simulate the operation of a planar 5 MHz array with 64 elements (full details shown in Table 1). The output of each element, $s(t)$, was a five cycle, Gaussian windowed tone burst with a centre frequency of 5 MHz and a −6 dB bandwidth of 50%. The frequency spectrum, $S(\omega)$, can be calculated from the element output signal using the Fourier transform as follows:

$$S(\omega) = \int_{-\infty}^{\infty} s(t)e^{-i\omega t}dt. \tag{6}$$

A directivity function D was used to describe the angular distribution of the ultrasonic field for each array element. In the far field, this function is given by [1]:

$$D(\omega, \theta) = \frac{(c_L/c_S)^2 - 2\sin^2\theta}{\Phi(\sin\theta)}\ \sin\ c\left(\frac{\omega b\ \sin\ \theta}{2c_L}\right)\cos\ \theta, \tag{7}$$

where b is the width of an array element, θ is the angle with respect to the element normal, c_L and c_S are the bulk longitudinal and shear wave velocities in the medium and

$$\Phi(\zeta) = \left(2\zeta^2 - (c_L/c_S)^2\right)^2 - 4\zeta^2(\zeta^2 - 1)^{1/2}(\zeta^2 - (c_L/c_S)^2)^{1/2}. \tag{8}$$

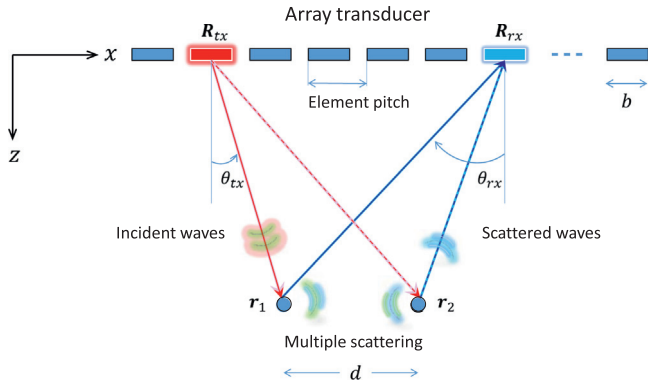

Fig. 1. Schematic diagram of the array and scatterer geometry.

Table 1
Model and experimental array parameters.

Array parameter	Value
Element number	64
Element width	0.53 mm
Element pitch	0.63 mm
Centre frequency	5 MHz
Bandwidth (−6 dB)	50%

The incident field on each point scatterer is considered as

$$\phi^{in}(\boldsymbol{r}_j) = D_{tx} G_j^{tx} S(\omega), \quad (j = 1, 2), \tag{9}$$

where $D_{tx} = D(\omega, \theta_{tx}), G_j^{tx} = G(\boldsymbol{r}_j, \boldsymbol{R}_{tx}), tx$ refers to the transmitter, and $S(\omega)$ accounts for the transfer function of the emitted pulse. The resulting spectrum for each transmitter–receiver pair, $H_{tx,rx}(\omega)$, is given by:

$$H_{tx,rx}(\omega) = \left[G_1^{rx} f_1 \phi_1^{ex}(\boldsymbol{r}_1) + G_2^{rx} f_2 \phi_2^{ex}(\boldsymbol{r}_2)\right] D_{rx}, \tag{10}$$

where $D_{rx} = D(\omega, \theta_{rx}), G_j^{rx} = G(\boldsymbol{R}_{rx}, \boldsymbol{r}_j), rx$ refers to the receiver, and ϕ_j^{ex} are calculated by substituting Eq. (9) into Eq. (4) and solving to give:

$$\phi_1^{ex}(\boldsymbol{r}_1) = D_{tx} \frac{G_1^{tx} + f_2 G(\boldsymbol{r}_1, \boldsymbol{r}_2) G_2^{tx}}{1 - f_1 f_2 G(\boldsymbol{r}_1, \boldsymbol{r}_2) G(\boldsymbol{r}_2, \boldsymbol{r}_1)} S(\omega), \tag{11a}$$

$$\phi_2^{ex}(\boldsymbol{r}_2) = D_{tx} \frac{G_2^{tx} + f_1 G(\boldsymbol{r}_2, \boldsymbol{r}_1) G_1^{tx}}{1 - f_1 f_2 G(\boldsymbol{r}_1, \boldsymbol{r}_2) G(\boldsymbol{r}_2, \boldsymbol{r}_1)} S(\omega). \tag{11b}$$

The scattering coefficients f_j are determined by imposing appropriate boundary conditions on the surface of each scatterer; they are complex-valued and frequency dependent.

In the remainder, we assume that both scatterers are identical circular holes of size a (x–z plane) and infinite length in the Y-direction, so that

$$f \equiv f_j = \frac{i\pi}{4}\left(\frac{c_L^2}{c_S^2} - 1\right)\tilde{\omega}^2, \quad \text{where} \quad \tilde{\omega} = ka \ll 1. \tag{12}$$

Note that the simplest way to calculate the resulting spectrum is to consider the situation of 'single scattering'. In this case, it is assumed that the exciting field on each scatterer is equal to the incident field, thus any interaction between the scatterers is ignored. Then, corresponding to expression (10), one finds that:

$$H_{tx,rx}(\omega) = f D_{tx}\left(G_1^{tx} G_1^{rx} + G_2^{tx} G_2^{rx}\right) D_{rx} S(\omega). \tag{13}$$

The raw time-domain signal, $h_{tx,rx}(t)$, recorded by a receiving element at $\boldsymbol{R}_{rx}$ when an element at $\boldsymbol{R}_{tx}$ is transmitter, is the inverse Fourier transform of $H_{tx,rx}(\omega)$. This process is carried out for each possible transmitter–receiver pair to produce N^2 time domain signals which make up the FMC data although reciprocity means that there are only $N(N+1)/2$ independent signals. Finally, it should be noted that one aspect not captured in this model is mode conversion at the scatterers due to the simplifying assumption of a scalar wave equation. However, as the purpose of the model is to explore the effect of high noise levels on imaging performance, it seems unlikely that this approximation affects the conclusions.

3. Post-processing algorithms

3.1. Total focusing method

The TFM [17] is a delay and sum beamforming algorithm, in which the array is synthetically focused on each image point $\boldsymbol{r}$ in the imaging region (x–z plane). For this reason, the TFM can yield the highest possible imaging resolution of any linear algorithm and has been termed the 'gold standard' in array imaging [37]. For an array in direct contact with the medium, the image intensity $I(\boldsymbol{r})$, can be written as:

$$I(\boldsymbol{r}) = \left|\sum h_{tx,rx}\left(\frac{|\boldsymbol{R}_{tx} - \boldsymbol{r}| + |\boldsymbol{R}_{rx} - \boldsymbol{r}|}{c_L}\right)\right|, \tag{14}$$

where the summation is over all possible transmitter–receiver combinations and so all the N^2 time domain signals contribute to the image. The effect of using c_L in the above equation is to dramatically reduce the influence of any shear waves present on the image results, hence why it was reasonable to neglect them in the forward model.

3.2. Time-reversal with multiple signal classification

Time-reversal MUSIC [21,26–33] is a widely used super resolution imaging algorithm. This method starts by defining the time-reversal matrix T:

$$T(\omega_c) = H_{tx,rx}^{*t}(\omega_c) H_{tx,rx}(\omega_c), \tag{15}$$

where ω_c is typically the centre frequency of the transducer and the superscript '$*t$' denotes the complex conjugate transpose of the matrix.

The singular values σ_i, and singular vectors, μ_i, of matrix $T(\omega_c)$, which forms the basis of time-reversal MUSIC imaging, are obtained from the full matrix of transmit–receive signals *via* singular value decomposition. Since the time-reversal matrix $T(\omega_c)$ is a Hermitian matrix, the singular values are real and singular vectors are orthogonal.

We then divide the singular vectors into two parts: signal subspace U_S and noise subspace U_N:

$$U_S = [\mu_1, \mu_2, \cdots\cdots, \mu_m], \tag{16a}$$

$$U_N = [\mu_{m+1}, \mu_{m+2}, \cdots\cdots, \mu_N], \tag{16b}$$

where m is the number of nonzero singular values. In practice, due to the presence of noise, all singular values are larger than zero, so a threshold is defined to discriminate the singular values corresponding to signal and noise, typically those singular vectors corresponding to singular values below 10% of the largest are assumed to belong to the noise space. It is worth noting that the value of this threshold is arbitrary and so should be tuned depending on the test structure and defects of interest.

Imaging is achieved through a steering vector, which for each image point $\boldsymbol{r}$, is given by:

$$g(\boldsymbol{r}) = [G(\boldsymbol{R}_1, \boldsymbol{r}), G(\boldsymbol{R}_2, \boldsymbol{r}), \cdots\cdots, G(\boldsymbol{R}_N, \boldsymbol{r})], \tag{17}$$

where $\boldsymbol{R}_l (l = 1, 2, \ldots, N)$ are array element centre positions and G is the relevant Green's function of the medium, i.e., Eq. (1). The intensity $I(\boldsymbol{r})$, at image point $\boldsymbol{r}$ is then:

$$I(\boldsymbol{r}) = \frac{1}{\sum_{j=m+1}^{N} \left|\left\langle \mu_j^*, g(\boldsymbol{r}) \right\rangle\right|^2}, \tag{18}$$

where the angle brackets $\langle\ \rangle$ represent the inner product. Note that Eq. (18) is a search algorithm which returns a high value when $g(\boldsymbol{r})$ is orthogonal to the singular vectors in the noise space which happens when a reflector is located at the search location.

3.3. Performance indicators

Here we quantitatively compare the performance of imaging algorithms in terms of resolution and robustness to noise, which are two important performance indicators for NDE imaging algorithms since both impact the ability to perform defect detection, characterisation and sizing. In this paper, two parameters termed the peak to centre intensity difference and the array performance indicator (API) [17] are introduced to aid this quantification.

The peak to centre intensity difference, τ, is defined in Fig. 2(d) and quantifies the ability of an imaging algorithm to separate two closely spaced targets. Fig. 2(a–c) shows the simulated results of TFM images of two 1 mm-diameter circular scatterers located at $(x = \pm 0.85\lambda,\ z = 39\lambda)$, $(x = \pm 0.7\lambda,\ z = 39\lambda)$ and $(x = \pm 0.5\lambda,\ z = 39\lambda)$ where λ is the wavelength at the central frequency of 5 MHz. Fig. 2(d–f) shows the cross sections of the images taken through the centres of the two scatterers (i.e. at $z = 39\lambda$). If some

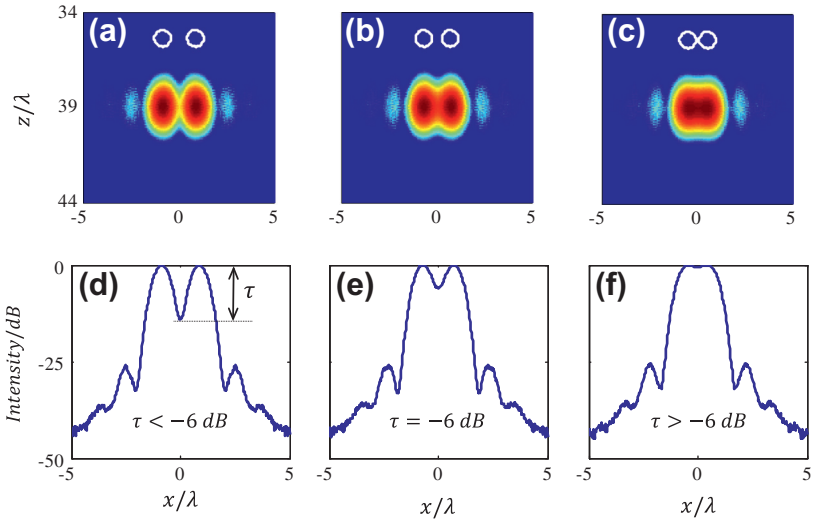

Fig. 2. Simulated TFM images: (a and d) for $d = 1.7\lambda$; (b and e) for $d = 1.4\lambda$; (c and f) for $d = \lambda$. Top figures are TFM images; bottom figures are sections taken through the images at $z = 39\lambda$ (all results are displayed with a −40 dB dynamic range).

arbitrary threshold is passed, e.g., $\tau < -6$ dB, the two scatterers are typically considered to be resolved, as shown in Fig. 2(a and d). If $\tau > -6$ dB, the two scatterers cannot be resolved as shown in Fig. 2(c and f).

The array performance indicator (API) is used to measure the area of the image of the target(s) and is defined as [17]:

$$\mathrm{API} = \frac{\mathrm{Area}_{-6\ \mathrm{dB}}}{\lambda^2} \tag{19}$$

where $\mathrm{Area}_{-6\ \mathrm{dB}}$ is the area of the image, within which the amplitude is greater than −6 dB of its maximum value in the defined imaging area.

In order investigate the effects of noise, Gaussian white noise is introduced to the model and is added to the recorded time domain signals. The signal to noise ratio (SNR) in dB was measured in the time domain and defined by:

$$\mathrm{SNR} = 20\log_{10}\frac{A_{\mathrm{signal\ peak}}}{A_{\mathrm{noise\ RMS}}} \tag{20}$$

where $A_{\mathrm{signal\ peak}}$ is the peak amplitude of signal reflected from defects and $A_{\mathrm{noise\ RMS}}$ is the RMS the noise measured away from the region of signal.

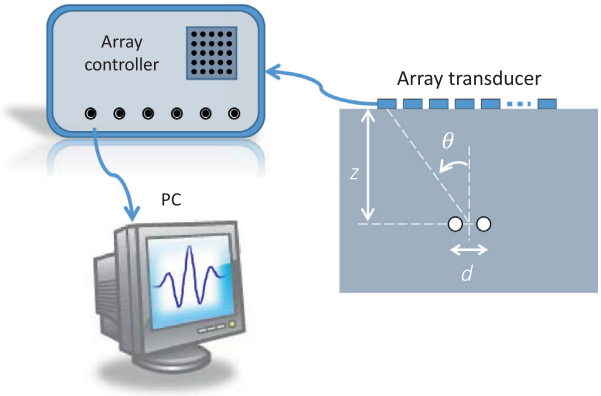

Fig. 3. Schematic diagram of the experimental apparatus.

4. Experimental validation

4.1. Experimental apparatus

An experimental system was designed and built as shown in Fig. 3. A commercial array controller (manufactured by Peak NDT Ltd., UK), was connected to a standard PC. The array controller has 128 independent channels, each with 16 bit digitization. A commercial ultrasonic linear array (manufactured by Imasonic, France) was used which had 64 elements with a centre frequency of 5 MHz (full array details showed in Table 1, and the array controller details in Table 2). Note that the size of the array elements in the *Y*-direction was 15 mm (or 12λ) making the two-dimensional approximation used in the model reasonable.

To validate the performance of TFM and time-reversal MUSIC under different noise levels, steel and copper samples were used in the experiment (the details shown in Table 3). Two side-drilled holes (SDHs) of radius $a = 0.5$ mm were machined in both sample materials as shown in Fig. 3. Note that both steel and copper are isotropic materials, and copper exhibits a high degree of material backscatter.

4.2. Effects of multiple scattering

Multiple scattering exists in the experiment. Here we use the model described in Section 2 to switch multiple scattering on and off and so explore its effects on the imaging algorithms.

Fig. 4(a) shows the simulated and experimental TFM images of scatterers in steel. The imaging results labelled 'single scattering' and 'multiple scattering' are simulated results of two 1 mm-diameter circular scatterers, located at $(x = -1.3\lambda,\ z = 39\lambda)$ and $(x = 1.3\lambda,\ z = 39\lambda)$. The imaging result labelled 'experiment' is obtained from the two side-drilled holes with diameters of 1 mm and

Table 2
Array controller settings.

Parameter	Value
Pulse width	80 ns
Pulse voltage	100 V
Sample frequency	50 MHz
Sample points	1600
Amplifier gain	40 dB

Table 3
Sample parameters.

Parameter	Steel	Copper
Velocity (m/s)	5747.1	4673.1
Wavelength @ 5 MHz (mm)	1.1	0.9
Defect position (A)	(d = 1.2, z = 22 or 39)	
	(d = 1.7, z = 22 or 39)	(d = 1.7, z = 22)
	(d = 2.6, z = 22 or 39)	(d = 2.6, z = 22)
	(d = 3.5, z = 22 or 39)	(d = 3.5, z = 22)

the same position as in the model. In the model, Gaussian white noise, resulting in a time domain SNR of 30 dB, was added. Fig. 4(b) shows lateral cross sections through the centre of the two targets from which it can be seen that the effect of multiple scattering on the TFM is small and does not affect the lateral resolution. The most significant effect of multiple scattering on the TFM images can be seen in Fig. 4(a) as a low amplitude 'tail' below the scatterers in the regions indicated by the dashed boxes.

Fig. 5(a) shows the simulated results of two point-like scatterers, located at $(x = -\lambda/6,\ z = 39\lambda)$ and $(x = \lambda/6,\ z = 39\lambda)$, imaged using time-reversal MUSIC. In the model, Gaussian white noise, which results in a time domain SNR of 30 dB, was added. Fig. 5(b) shows lateral cross sections through the centre of the two scatterers. Simulated results were obtained at a single frequency of 5 MHz, which is equal to the central frequency of the array used in the experiments. Note that the filter used in the TFM imaging was also centred on 5 MHz. From Fig. 5 it can be seen that the image when multiple scattering was included has somewhat improved lateral resolution (over the single scattering case) and the point scatterers separated by $\lambda/3$ are just resolvable. This additional resolution stems from the improved performance of the time reversal process in the presence of multiple scattering [34].

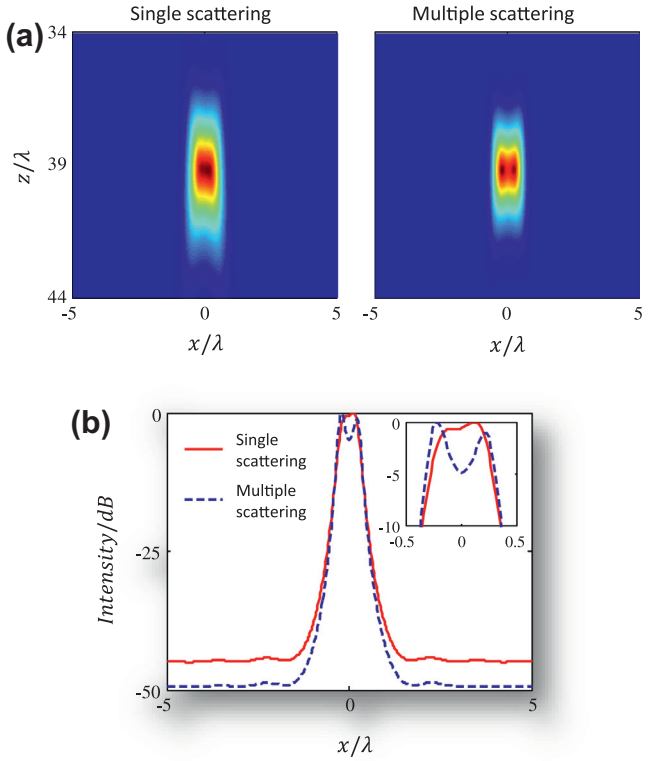

Fig. 5. Simulated time-reversal MUSIC images of two scatterers located at $z = 39\lambda$ and $d = \lambda/3$, (a) shows the time-reversal MUSIC images (all results are displayed with a −40 dB dynamic range) and (b) shows lateral cross sections through the centre of targets ($z = 39\lambda$).

4.3. Experimental lateral resolution

Lateral resolution is defined as the ability of an imaging algorithm to distinguish two targets in the direction perpendicular to the direction of the ultrasonic beam. The experiment performed on the steel sample was used to compare resolution of the imaging algorithms, using the experimental setup shown in Fig. 3.

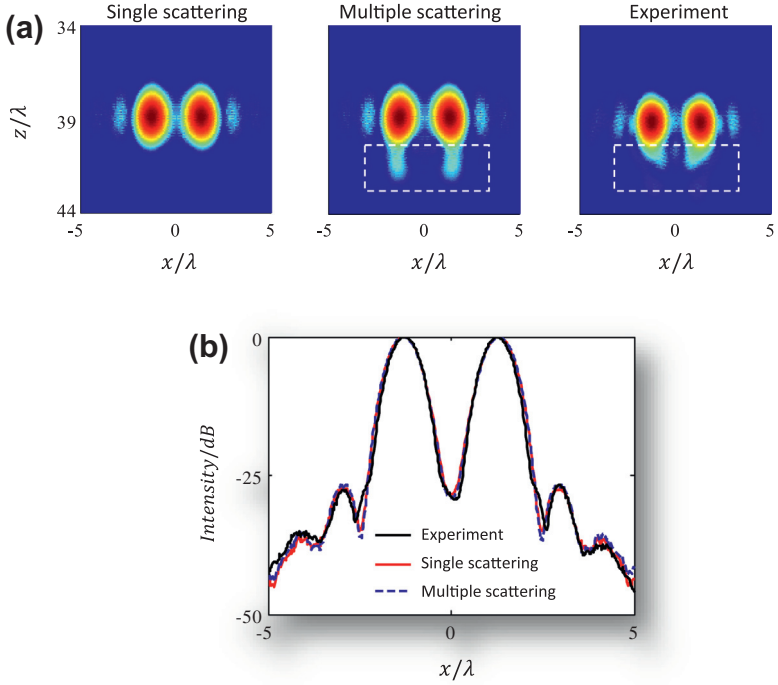

Fig. 4. TFM images from model and experimental data for two targets in the steel sample (two circular scatterers in the model and two SDHs in the experiment) located at $z = 39\lambda$ and $d = 2.6\lambda$, (a) shows the TFM images (all results are displayed with a −40 dB dynamic range) and (b) shows lateral cross sections through the centre of targets ($z = 39\lambda$).

According to the Rayleigh criterion [38], for the sample and array geometry shown in Fig. 3, the Rayleigh limit, L, (or minimum resolvable distance) of imaging system, at $z = 39\lambda$, is given by:

$$L = \frac{0.61\lambda}{\sin(\theta)} = 1.5\lambda \tag{21}$$

Fig. 6(a) shows the experimental lateral cross sections through the centre of the two SDHs in the steel sample. Fig. 6(b) shows the peak to centre intensity difference, τ, as a function of the central distance between two SDHs. If $d > L$, both TFM and time-reversal MUSIC can be seen to resolve the two SDHs. Conversely, if $d < L$, TFM is diffraction limited as expected and time-reversal MUSIC is seen to overcome this limit.

4.4. Noise

There are two types of noise that need to be considered in the experiment: electronic and material noise [39]. Electronic noise consists of thermal and digitization noise, and is uncorrelated with time. Therefore electronic noise can be reduced by averaging over time. Material noise, caused by material backscattered energy, is correlated over time and is the limiting factor in most ultrasonic defect detection scenarios (see for example the work of Bernard Hosten on composites [40]).

Gaussian white noise with different SNRs is introduced into the model to explore the performance of different imaging algorithms. Note that as the noise we add is random, twenty repetitions of each SNR case were carried out and the RMS values of the performance indicators τ and API are taken. The imaging results for different SNRs were obtained in an area of $10\lambda \times 10\lambda$, centred on the two scatterers.

Fig. 7 shows τ and API, calculated from simulation results, as a function of SNR for different scatterer separation distances, d. It is clear that if SNR > 20 dB, both the τ and API obtained from the time-reversal MUSIC images are lower than that obtained from the TFM images. This suggests that for high SNRs, time-reversal MUSIC imaging out-performs TFM. As the SNR decreases, the τ and API obtained from time-reversal MUSIC can be seen to increase whereas those from TFM remain stable. If SNR < 5 dB, time-reversal MUSIC performs particularly poorly with τ tending to zero, the API increasing sharply and the presence of unwanted imaging artefacts.

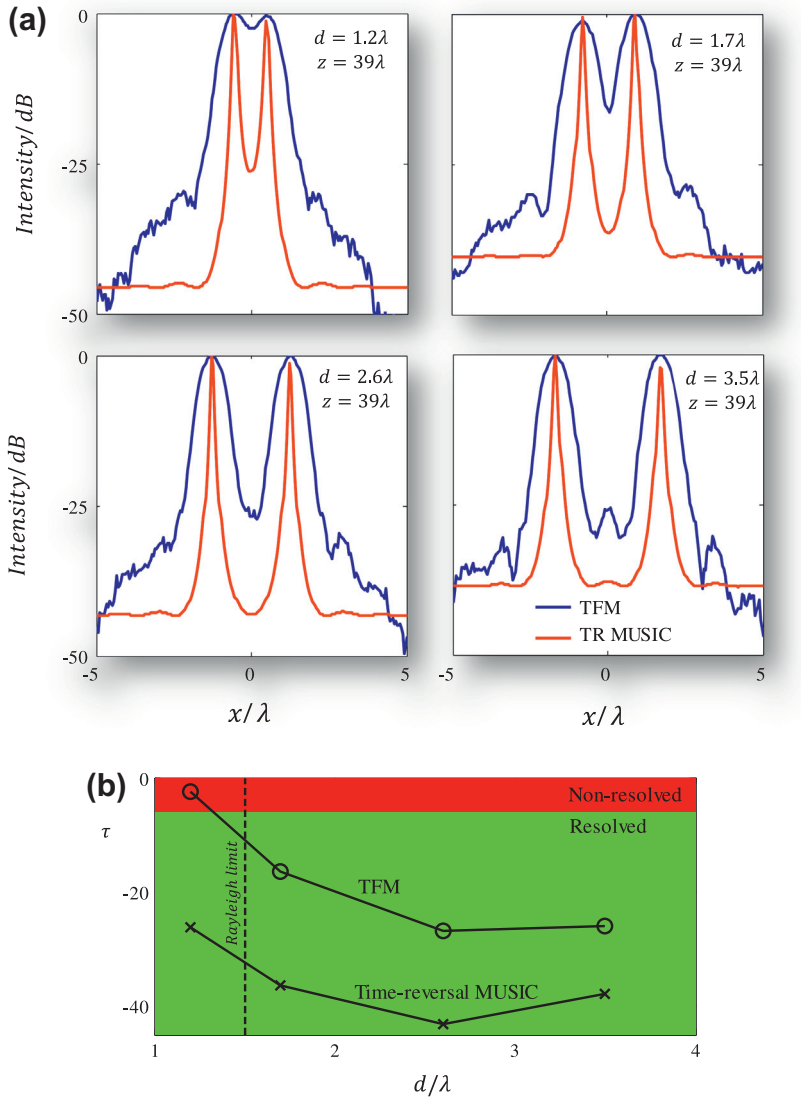

Fig. 6. Experimental results in the steel sample: (a) lateral cross sections where the red lines are TR-MUSIC and the blue lines are TFM and (b) peak to centre intensity difference, τ, as a function of separation, d. (For interpretation of the references to colour in this figure legend, the reader is referred to the web version of this article.)

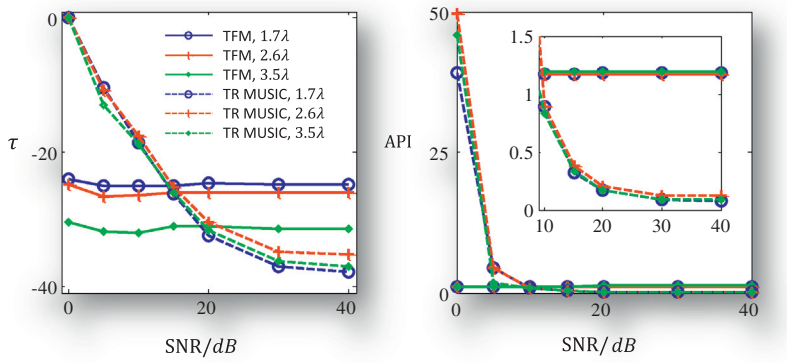

Fig. 7. Comparison of the imaging performance of TFM and time-reversal MUSIC for simulated data with various levels of added noise.

Experiments in steel and copper, which have different SNR levels, were performed to verify the above simulated results. Fig. 8(a and b) shows the pulse–echo time domain signals (i.e. transmitting and receiving on the same array element) in the steel sample for 5 MHz and 2.5 MHz arrays. From Fig. 8(a and b), the signals reflected from the scatterers can be seen along a parabolic arc. Note that for the steel samples the SNR was always in excess of 30 dB. Fig. 8(c and d) shows the equivalent results for the copper sample. In this case the SNR at 5 MHz is less than 0 dB and the location of the defects is only visible at 2.5 MHz where the grain scatter is reduced.

Fig. 9(a and b) shows experimental imaging results in steel and copper using TFM and time-reversal MUSIC with different separations (in both cases greater than the Rayleigh limit). It can be seen that the scatterers can be located in steel and copper using the TFM imaging algorithm. To make the comparison between results on these different materials fair, the array size, and hence its numerical aperture, was set at a fixed number of wavelengths by using all 64 elements on the steel sample and reducing this to 50 for copper (note that in both cases the array detailed in Table 1 was used). From Fig. 9 is apparent that for a given algorithm the shape of the imaged scatterer is similar (approximately circular for TFM and elliptical for time-reversal MUSIC). However, as noise increases from the steel to the copper sample so the size of the imaged target for the time-reversal MUSIC algorithm increases markedly. The time-reversal MUSIC algorithm also exhibits various image artefacts, which would generate unwanted false positives in any NDE assessment.

Table 4 shows the API from the experiments in steel and copper, using TFM and time-reversal MUSIC. As shown in Table 4, the API obtained using TFM remains stable for the two materials, verifying the predicted robustness of TFM to relatively high noise. Conversely, the API for time-reversal MUSIC is seen to be significantly degraded by the low SNR of the copper sample in-line with predictions.

Fig. 10 explores the effect of the arbitrary threshold used to distinguish the noise and signal spaces in time-reversal MUSIC. Here the input data is that from the copper sample with an SNR less than 0 dB. Fig. 10 shows images for thresholds of 2.5% and 30% which can be compared with Fig. 9 for a 10% threshold. This comparison

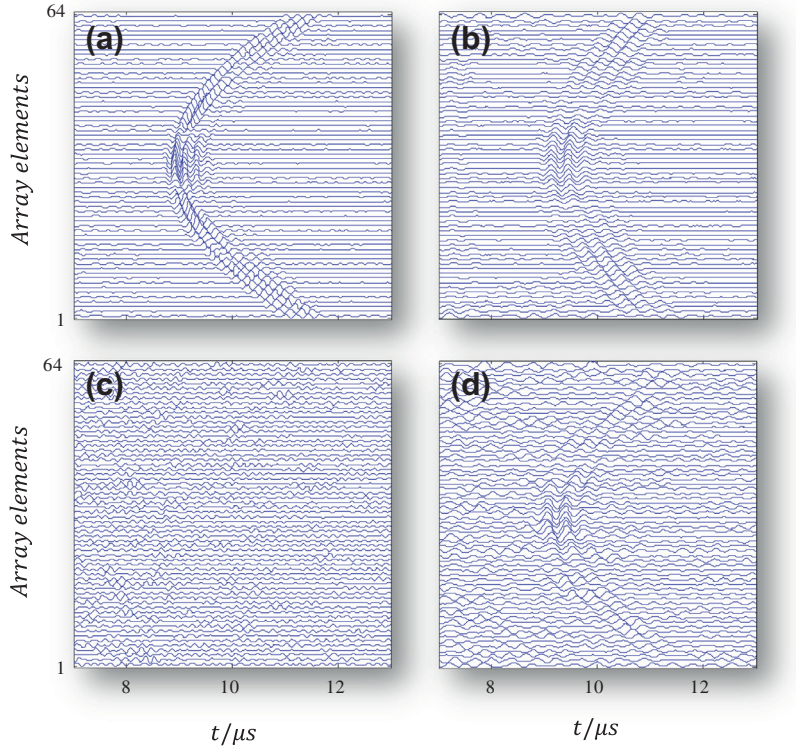

Fig. 8. Pulse–echo time domain data from (a) steel at 5 MHz, (b) steel at 2.5 MHz, (c) copper at 5 MHz and (d) copper at 2.5 MHz.

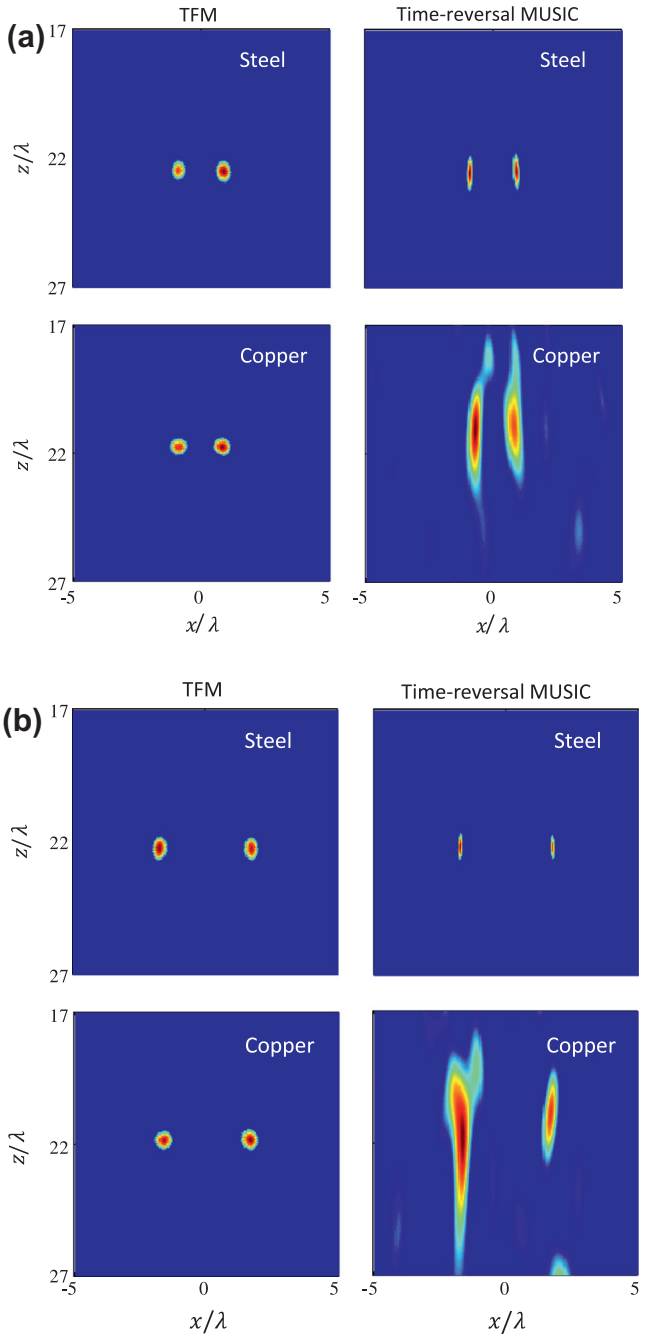

Fig. 9. Experimental results in steel and copper using TFM and time-reversal MUSIC with (a) $d = 1.7\lambda$ and (b) $d = 3.5\lambda$ (all results are displayed with a -6 dB dynamic range).

Table 4
Experimental API in steel and copper samples using TFM and time-reversal MUSIC algorithms.

Material	TFM	Time-reversal MUSIC
Steel	0.89 ($d = 1.7\ \lambda$)	0.76 ($d = 1.7\ \lambda$)
	1.03 ($d = 2.6\ \lambda$)	0.82 ($d = 2.6\ \lambda$)
	0.96 ($d = 3.5\ \lambda$)	0.41 ($d = 3.5\ \lambda$)
Copper	0.91 ($d = 1.7\ \lambda$)	21.46 ($d = 1.7\ \lambda$)
	1.10 ($d = 2.6\ \lambda$)	13.13 ($d = 2.6\ \lambda$)
	0.99 ($d = 3.5\ \lambda$)	24.93 ($d = 3.5\ \lambda$)

reveals that the 10% threshold provides the best image for this sample and defect combination. The algorithm will only work

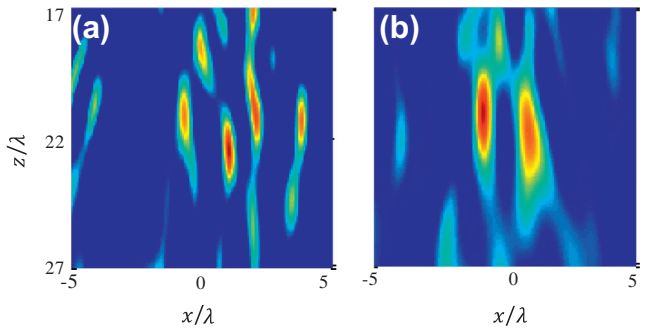

Fig. 10. Effect of the threshold in time-reversal MUSIC: images with thresholds at (a) 2.5% and (b) 30%. Here, $d = 1.7\lambda$ and both results are displayed with a -6 dB dynamic range.

effectively if the signal and noise spaces are correctly allocated and the presence of noise means that there is a less clear demarcation of these spaces. For the copper samples, as the threshold moves from 2.5% to 30% so the size of the noise space (N–m) varies from 11 to 37 respectively. Finally, note that the effect of this threshold is less significant for data with higher SNR levels where the signal and noise spaces are clearly demarked.

5. Conclusion

This paper compared the total focusing method, termed the gold standard in delay and sum beamforming, with the widely used time-reversal MUSIC super resolution technique. The comparison was in terms of ability to resolve closely spaced scatterers in a solid in the presence of noise, a key challenge in NDE. The ability to resolve closely spaced scatterers was assessed using the peak to centre intensity difference, τ, and the array performance indictor (API) was used to measure the area of the image of the targets. The model allowed multiple scattering between the targets to be introduced and this was found to produce very good agreement with experiment. The inclusion of multiple scattering was also shown to slightly improve the lateral resolution performance of the time-reversal MUSIC images whilst producing a small image artefacts in the TFM images. The experiments and simulations demonstrated the robustness of the TFM algorithm in the presence of noise even for a time domain SNR as low as 0 dB. When compared to the TFM at low noise cases (time domain SNR > 20 dB) the time-reversal MUSIC algorithm was shown to produce significantly improved lateral resolution (well below the classical diffraction limit) and compact point spread functions. For high noise levels the time-reversal MUSIC algorithm was shown to perform less well and its performance was very poor as the time domain SNR decreased below 5 dB. These results suggest that a sensible approach would be to monitor the SNR when using time-reversal MUSIC and if it falls below 20 dB compute the TFM in preference.

References

[1] B. Drinkwater, P. Wilcox, Ultrasonic arrays for non-destructive evaluation: a review, NDT E Int. 39 (2006) 525–541.
[2] B. Puel, D. Lesselier, S. Chatillon, P. Calmon, Optimization of ultrasonic arrays design and setting using a differential evolution, NDT E Int. 44 (2011) 797–803.
[3] M. Akhnak, O. Martinez, L.G. Ullate, F. Montero de Espinosa, 64 Elements two-dimensional piezoelectric array for 3D imaging, Ultrasonics 40 (2002) 139–143.
[4] O. Martínez, M. Akhnak, L.G. Ullate, F. Montero de Espinosa, A small 2D ultrasonic array for NDT applications, NDT E Int. 36 (2003) 57–63.
[5] J. Dziewierz, S.N. Ramadas, A. Gachagan, R.L. O'Leary, D.O. Thompson, D.E. Chimenti, Hexagonal array structure for 2D NDE applications, in: AIP Conference Proceedings, American Institute of Physics, 2010, pp. 825–830.
[6] D.J. Powell, G. Hayward, Flexible ultrasonic transducer arrays for nondestructive evaluation applications. II. Performance assessment of

different array configurations, IEEE Trans. Ultrason., Ferroelectrics Frequency Control 43 (1996) 393–402.
[7] S. Chatillon, G. Cattiaux, M. Serre, O. Roy, Ultrasonic non-destructive testing of pieces of complex geometry with a flexible phased array transducer, Ultrasonics 38 (2000) 131–134.
[8] J.R. Berriman, D.A. Hutchins, A. Neild, T.H. Gan, P. Purnell, The application of time-frequency analysis to the air-coupled ultrasonic testing of concrete, IEEE Trans. Ultrason., Ferroelectrics Frequency Control 53 (2006) 768–776.
[9] A. Gachagan, G. Hayward, S.P. Kelly, W. Galbraith, Characterization of air-coupled transducers, IEEE Trans. Ultrason., Ferroelectrics, Frequency Control 43 (1996) 678–689.
[10] B.W. Drinkwater, P.D. Wilcox, Ultrasonic arrays: a comparison between medical and NDE requirements, in: D.O. Thompson, D.E. Chimenti (Eds.), Review of Progress in Quantitative Nondestructive Evaluation, AIP Conference Proceedings, AIP, 27, 2008, pp. 770–777.
[11] C. Holmes, B. Drinkwater, P. Wilcox, The post-processing of ultrasonic array data using the total focusing method, Insight – NonDestr. Test. Cond. Monit. 46 (2004) 677–680.
[12] A. Velichko, P.D. Wilcox, An analytical comparison of ultrasonic array imaging algorithms, J. Acoust. Soc. Am. 127 (2010) 2377–2384.
[13] C.J. Martín-Arguedas, D. Romero-Laorden, O. Martínez-Graullera, M. Pérez-López, L. Gómez-Ullate, An ultrasonic imaging system based on a new SAFT approach and a GPU beamformer, IEEE Trans. Ultrason., Ferroelectrics, Frequency Control 59 (2012) 1402–1412.
[14] B.W. Drinkwater, R.T. Higuti, C.J. Martín, L.G. Ullate, D. Romero, M. Parrilla, et al., Improving synthetic aperture image by image compounding in beamforming process, in: D.O. Thompson, D.E. Chimenti (Eds.), Review of Progress in Quantitative Nondestructive Evaluation, AIP Conference Proceedings, American Institute of Physics, 30, 2011, pp. 728–735.
[15] N. Portzgen, D. Gisolf, G. Blacquiere, Inverse wave field extrapolation: a different NDI approach to imaging defects, IEEE Trans. Ultrason., Ferroelectrics Frequency Control 54 (2007) 118–127.
[16] N. Portzgen, D. Gisolf, D.J. Verschuur, Wave equation-based imaging of mode converted waves in ultrasonic NDI, with suppressed leakage from nonmode converted waves, IEEE Trans. Ultrason., Ferroelectrics, Frequency Control 55 (2008) 1768–1780.
[17] C. Holmes, B.W. Drinkwater, P.D. Wilcox, Post-processing of the full matrix of ultrasonic transmit–receive array data for non-destructive evaluation, NDT E Int. 38 (2005) 701–711.
[18] E. Betzig, A. Lewis, A. Harootunian, M. Isaacson, E. Kratschmer, Near field scanning optical microscopy (NSOM): development and biophysical applications, Biophys. J. 49 (1986) 269–279.
[19] A. Lewis, H. Taha, A. Strinkovski, A. Manevitch, A. Khatchatouriants, R. Dekhter, et al., Near-field optics: from subwavelength illumination to nanometric shadowing, Nat. Biotechnol. 21 (2003) 1378–1386.
[20] F.-C. Chen, W.C. Chew, Experimental verification of super resolution in nonlinear inverse scattering, Appl. Phy. Lett. 72 (1998) 3080.
[21] Y. Labyed, L. Huang, Ultrasound time-reversal MUSIC imaging with diffraction and attenuation compensation, IEEE Trans. Ultrason., Ferroelectrics, Frequency Control 59 (2012) 2186–2200.
[22] F. Simonetti, Localization of pointlike scatterers in solids with subwavelength resolution, Appl. Phys. Lett. 89 (2006) 094105.
[23] J.-L. Thomas, F. Wu, M. Fink, Time reversal focusing applied to lithotripsy, Ultrason. Imaging 18 (1996) 106–121.
[24] M. Fink, G. Montaldo, M. Tanter, Time-reversal acoustics in biomedical engineering, Annu. Rev. Biomed. Eng. 5 (2003) 465–497.
[25] C. Prada, E. Kerbrat, D. Cassereau, M. Fink, Time reversal techniques in ultrasonic nondestructive testing of scattering media, Inverse Probl. 18 (2002) 1761–1773.
[26] F.K. Gruber, E.A. Marengo, A.J. Devaney, Time-reversal imaging with multiple signal classification considering multiple scattering between the targets, J. Acoust. Soc. Am. 115 (2004) 3042–3047.
[27] E.A. Marengo, F.K. Gruber, F. Simonetti, Time-reversal MUSIC imaging of extended targets, IEEE Trans. Image Process. 16 (2007) 1967–1984.
[28] R. Schmidt, Multiple emitter location and signal parameter estimation, IEEE Trans. Anten. P. 34 (1986) 276–280.
[29] J.W. Odendaal, E. Barnard, C.W.I. Pistorius, Two-dimensional super resolution radar imaging using the MUSIC algorithm, IEEE Trans. Anten. P. 42 (1994) 1386–1391.
[30] T. Iwata, Y. Goto, H. Susaki, Application of the multiple signal classification (MUSIC) method for one-pulse burst-echo Doppler sonar data, Meas. Sci. Technol. 12 (2001) 2178–2184.
[31] C. Prada, J.-L. Thomas, Experimental subwavelength localization of scatterers by decomposition of the time reversal operator interpreted as a covariance matrix, J. Acoust. Soc. Am. 114 (2003) 235–243.
[32] M. Davy, J.G. Minonzio, J. de Rosny, C. Prada, M. Fink, Influence of noise on subwavelength imaging of two close scatterers using time reversal method: theory and experiments, Prog. Electromagn. Res. 98 (2009) 333–358.
[33] E.G. Asgedom, L.-J. Gelius, A. Austeng, S. Holm, M. Tygel, Time-reversal multiple signal classification in case of noise: a phase-coherent approach, J. Acoust. Soc. Am. 130 (2011) 2024–2034.
[34] F. Simonetti, Multiple scattering: the key to unravel the subwavelength world from the far-field pattern of a scattered wave, Phys. Rev. E 73 (2006) 036619.
[35] J. de Rosny, C. Prada, Comment on multiple scattering: the key to unravel the subwavelength world from the far-field pattern of a scattered wave, Phys. Rev. E 75 (2007) 048601.
[36] L.L. Foldy, The multiple scattering of waves. I. General theory of isotropic scattering by randomly distributed scatterers, Phys. Rev. 67 (1945) 107–119.
[37] M. Karaman, M. O'Donnell, Synthetic aperture imaging for small scale systems, IEEE Trans. Ultrason., Ferroelectrics Frequency Control 42 (1995) 429–442.
[38] J. Goodman, Introduction to Fourier Optics, Roberts and Company Publishers, 2004.
[39] R.Y. Chiao, L.J. Thomas, Analytic evaluation of sampled aperture ultrasonic imaging techniques for NDE, IEEE Trans. Ultrason., Ferroelectrics Frequency Control 41 (1994) 484–493.
[40] B. Hosten, M. Castaings, Transfer matrix of multilayered absorbing and anisotropic media. Measurements and simulations of ultrasonic wave propagation through composite materials, J. Acoust. Soc. Am. 94 (1993) 1488–1495.